

Will the Real Dynamic Instability
Mechanism Please Be Recognized!

L. E. Ericsson

Lockheed Missiles & Space Company, Inc.
Sunnyvale, California

There is a richness of flow mechanisms that can cause dynamic instability. Only after asking the right questions and carefully considering the answers can the fluid dynamic source of the observed dynamic instability be recognized. This will be illustrated by two carefully chosen examples.

In an aeroelastic test of a 25° swept wing with a symmetric airfoil section¹ (Fig. 1), violent oscillations in the first bending mode occurred if the location of boundary layer transition was not fixed (Fig. 2). The oscillations were of the limit cycle type, the typical result of nonlinear, negative aerodynamic damping (Fig. 3). What is the source of this dynamic instability?

The authors¹ propose a quasi-steady flow mechanism, which would require² that the transition-induced effect produces a net negative lift slope over at least the outboard wing sections. That is

$$C_{l\alpha} = (C_{l\alpha})_{FT} - (\Delta^i C_{l\alpha})_{TR} < 0 \quad (1)$$

where $(C_{l\alpha})_{FT}$ is the lift slope with fixed transition and $(\Delta^i C_{l\alpha})_{TR}$ is the lift loss due to free transition, which acts similarly to trailing edge stall (Fig. 4). The correct question to ask now is: "Can the resulting slope $C_{l\alpha}$ become negative and reach the magnitude needed to cancel the structural damping present in the test?" The experimental results for trailing edge stall³ (Fig. 5) show that negative lift slope results only at very high angles of attack, $\alpha > 12^\circ$ in Fig. 5. Even if the plunging-induced sectional angle of attack, \dot{z}/U_∞ exceeds the static stall angle, it is varying from $\alpha = 0$ to this maximum value beyond $\alpha = 12^\circ$, and positive damping is produced at $\alpha < 12^\circ$. As a matter of fact, even in the case of the much larger lift loss associated with leading edge stall (midgraph in Fig. 5), negative damping in plunge is only measured when the time average trim angle of attack α_0 is close to the static stall angle⁴ (Fig. 6), i.e., $\alpha_0 \approx \alpha_s$, not $\alpha_0 = 0$ as for the results in Figs. 2 and 3.

In order to find the real dynamic instability mechanism causing the divergent oscillations in Fig. 3 one needs to follow-up on the dynamic stall/dynamic transition analogy. Starting with the conceptually simpler case of pitch oscillations, accounting for the circulation lag and the effect on flow separation of the unsteady boundary layer edge conditions makes it possible to predict the measured negative damping at stall⁴ (Fig. 7a). However, the results⁶ in Fig. 7b show that this dynamic flow mechanism is incomplete. It cannot explain how a 6° pitch oscillation at $\alpha_0 = 22^\circ$ can cause the flow to attach to generate time-average lift high above static lift maximum, obtained at $\alpha \approx 10^\circ$. A dynamic flow mechanism is needed that can

energize the boundary layer developed between flow stagnation and separation points to the extent needed to prevent flow separation. The "leading-edge-jet" effect⁷ illustrated in Fig. 8 provides such a flow mechanism. As the airfoil leading edge moves upward during the "upstroke", the boundary layer is strengthened by the wall-jet-like moving wall effect and is more difficult to separate. The "rolling leading edge," used in Fig. 8 to illustrate the "leading edge jet" effect, has been investigated in detail⁸.

The moving wall effect is of significant magnitude only in the region near the stagnation point, where the boundary layer is thin and, therefore, very sensitive to this wall-jet-like action. A similar moving wall effect on boundary layer transition has been observed on airfoils. Figure 8 illustrates how the plunging and pitching airfoils will have opposite moving wall effects for increasing effective angle of attack, \dot{z}/U_∞ and θ , respectively. Carta's hot film response data⁹ (Fig. 9)* show how the adverse (upstream) moving wall effect $\dot{z}(t)$ promotes transition and causes the plunging airfoil to have a longer run of attached turbulent flow prior to stall. As a result, the flow stays attached past 7.5% chord, whereas flow separation occurs forward of 5% chord on the pitching airfoil, which has a shorter turbulent run before stall due to the opposite, transition-delaying, moving wall effect. In addition to showing the opposite moving wall effects for pitching and plunging oscillations, Fig. 9 also demonstrates that the moving wall effect completely dominates over the accelerated flow effect, i.e., the effect of the lessened leeside pressure gradient adversity⁸, which is the same for pitching and plunging oscillations. This dominance is found in numerous flow situations both in two-dimensional and three-dimensional flow¹⁰.

The plunging airfoil section of the wing in Figs. 1-3 will experience a transition-promoting moving wall effect on the top side during the "down stroke" of the bending oscillation. On the bottom side, the moving wall effect is the opposite, delaying transition. As a result, a negative lift component is generated which drives the oscillation (Fig. 10). The question one now must ask is: "How can the transition asymmetry generated by the moving wall effect produce a negative load that dominates over the attached flow load, $C_{l\alpha} \dot{z}/U_\infty$, when it could not in the quasi-steady case discussed earlier, (Eq. (1))?" In the latter case, transition reacts to the change of the pressure gradient at the boundary layer edge due to \dot{z}/U_∞ . The test results⁹ in Fig. 9 show that the (viscous) moving wall effect completely dominates over this inviscid pressure gradient effect, providing the answer to the question raised.

Wing bending oscillations of the limit cycle type, similar to those for the 25° swept wing (Figs. 1-3), have also been observed on a highly swept wing¹¹ (Fig. 11). The measured damping shows that the dominant dynamic flow mechanism changed when decreasing the wing sweep to $\Lambda = 55^\circ$ or less (Fig. 12). The characteristics shown in Fig. 13 rule out shock-induced flow separation as a source of the self-excited oscillation, as was also concluded in Ref. 11, where it was suggested that one or both of the following vortex-induced effects was the source (see Fig. 14). In one case (left diagram), the suggested source is the changing strength of the leading-edge vortex with increasing angle of attack, which due to the associated phase lag can generate a dynamically destabilizing lift component. The mechanism would

*The amplitudes of $\dot{z}(t)/U_\infty$ and $\theta(t)$ are of the same magnitude.

be similar to that for the "spilled" leading-edge vortex in dynamic airfoil stall^{7,12}. In the other case (right diagram), the suggested flow mechanism is the breakdown of the leading-edge vortex.

The obvious question that must be answered affirmatively before suggesting candidate flow mechanisms, such as those shown in Fig. 14, is if they can produce the observed data trends (Figs. 12 and 13). In the present case they cannot. The "spilled" leading edge vortex (left diagram in Fig. 14) should cause a dynamically destabilizing effect that increases with increasing angle of attack, as the vortex strength increases. The start of cross flow separation occurs much earlier than at $\alpha = 7^\circ$, where the dynamic instability occurs. That is, the proposed flow mechanism could not produce the observed critical dependence upon angle of attack, limiting the dynamic instability to $7^\circ < \alpha < 10^\circ$ (Fig. 12). The vortex breakdown mechanism (right diagram in Fig. 14) will have a critical angle of attack associated with it; the angle at which breakdown starts occurring on the wing. However, this angle is well beyond $\alpha = 10^\circ$ for $\Lambda \geq 65^\circ$, according to the results obtained by Lambourne and Bryer¹³ for a swept wing (Fig. 15). One additional requirement would have been that the phase lag is 180° larger than in the first case (left diagram), as vortex burst causes a loss of lift. Thus, none of the suggested flow mechanisms can have caused the observed self-excited bending oscillations of the highly swept wing.

The photograph of the model¹¹ (Fig. 16) shows that the variable-sweep, thin outboard wing is preceded by a fixed sweep (67.5°) thick inboard wing or glove. The difference in leading edge radii is illustrated further by the cross-sectional diagram in Fig. 17. Even for the same leading edge sweep angle, the inner and outer wings will start generating leading edge vortices at different angles of attack because of the difference in their leading edge roundness¹⁴. Using the stall angles for 12% and 9% thick airfoils³ to represent the inner and outer wings, respectively, one finds that for 67.5° L.E. sweep the respective wings should start developing leading edge vortices at 6.3° and 4.5° . Compressibility-induced apparent sharpening of the leading edge could probably make the very thick inner wing glove (Fig. 17) act as a 12% thick airfoil in incompressible flow, whereas the leading edge of the outer wing becomes practically sharp, causing vortex development to start at $\alpha > 0$. Thus, considering that the inner vortex must gain some strength before it can interact with the outer wing vortex, one can see how the critical α -value shown in Fig. 13 can result. That leading edge roundness does delay the generation of a leading edge vortex, in the manner described in Ref. 14, was shown by comparison with experimental results¹⁵.

When the inner wing starts developing a leading edge vortex, it will trail inboard of the already existing leading edge vortex on the outer wing. That is, the situation is similar to the one existing for a double-delta wing¹⁶ (Fig. 18). The figure shows how the oil flow visualization results are correlated with the position of the (primary) leading edge vortices from outer and inner delta wing leading edges. The measured suction peaks indicate the locations of the vortices. When the angle of attack is increased above a certain critical value, the outer and inner leading edge vortices start to interact with each other, as is illustrated by the oil flow pictures¹⁷ in Fig. 19. At $\alpha = 5^\circ$, the two vortices are separate, as in Fig. 18. At $\alpha = 7^\circ$, however, the two vortices have started to interact (Fig. 19b), and at $\alpha = 10^\circ$ (Fig. 19c) they have combined into one vortex.

When one compares the flow visualization pictures for the double-delta wing planform (Fig. 19) with the oil flow visualization for the swept wing¹¹ one can see certain similarities. However, a more direct comparison, quantitative rather than qualitative, can be made by comparing the experimental pressure distributions for the double-delta plan form¹⁹ (Fig. 20) and the swept wing¹⁷ (Fig. 21). Figure 20 shows that the inner delta wing vortex, when it interacts with the vortex on the outer wing, causes the sectional loading to increase and shift its center inboard. Noticing that to the spanwise inboard movement for the delta wing¹⁷ (Fig. 20) corresponds a chordwise aft movement on the swept wing¹ (Fig. 21), one can conclude that the inner-outer vortex interactions do indeed cause very similar changes in the load distributions. The oscillation occurred when the load distribution in Fig. 21 changed from that typical for a single leading edge vortex ($\alpha = 6.9^\circ$) to that typical for the interaction discussed earlier ($\alpha = 8^\circ$).

The interaction between inner and outer wing vortices, described above, fits the experimental facts in regard to the observed bending oscillation of the swept wing¹¹ (Fig. 12). Thus, it produces a critical α - range in which the single vortex loading is being transformed to that resulting from the two interacting vortices. At higher angles of attack, the two vortices are merged into one vortex, and no self-excited bending oscillation will result. Furthermore, the large amplitude pressure oscillations are localized to the wing region where one expects the interaction between the two corotating vortices to take place¹¹ (Fig. 22).

Figure 23 shows the measured¹ spanwise variation of the local, streamwise angle of attack for $\Lambda = 67.5^\circ$ and a fuselage angle of attack of $\alpha = 7.38^\circ$. The solid line shows the variation due to static loads, and the dash-dot lines shows the extreme values $\alpha_0 + \Delta\alpha$ and $\alpha_0 - \Delta\alpha$ during the down- and up-stroke portions of the bending oscillations. The inner, thick wing-glove is at the constant angle of attack α_0 . Consequently, the effective apex of the outer wing does not move, and the only effect of the leading edge vortex is the entrainment-enhancement of the attached flow loads.¹⁸ If one approximates the α_0 - curve in Fig. 23 with a straight line, one could apply the analysis method of Ref. 18 directly. In any case, the single leading edge vortex will increase the damping in pitch for the rigid delta wing and the damping in bending for the present swept wing at a rate proportional to $\sin \alpha$. This is essentially the single vortex data trend exhibited in Fig. 12. The deviation is the interaction at $7^\circ < \alpha < 9^\circ$ between inner and outer vortices. It is also likely to be minor variations due to shock-boundary layer interaction¹⁹. Thus, what remains is to describe how the vortex interaction at $7^\circ < \alpha < 9^\circ$ can cause negative aerodynamic damping. Although the interaction is likely to generate a forcing function (buffet) due to general flow unsteadiness, the large amplitude response is caused by negative aerodynamic damping.

Whereas the single vortex effect is almost exclusively due to changing vortex strength, at least in regard to longitudinal aerodynamics, such as the pitch damping for a delta wing¹⁸ or the damping in bending for the present swept wing, in the case of the outer-inner vortex interaction the spanwise movement of the leading edge vortex on the outer wing becomes important. It has been shown by Randall²⁰ that the leading edge vortex describes spanwise oscillations around its static position (Fig. 24). Thus, during the α - increasing part of the pitch oscillation, the vortex is outboard of its

static position, and during the α -decreasing part it is inboard. The spanwise location of the leading edge vortex for stepwise changing angle of attack is shown in Fig. 25 for a very slender delta wing.²¹ The figure shows that for the moderate angle of attack range of interest in the present case, the spanwise location of the vortex is very sensitive to angle of attack. This explains the narrow α -range for outer-inner vortex interaction of the present swept wing.

With the aid of Figs. 21, 23 and 24 one can see how, when the wing angle of attack is increasing, the load distribution will change toward the front-loaded one for the undisturbed wing leading edge vortex. Conversely, the change will be towards the aft-loaded one, generated by the interaction from the glove vortex, when the angle of attack is decreasing. Figure 23 shows that the streamwise angle of attack of the swept wing is decreasing during the bending upstroke, $0 < \omega t < \pi$, and increasing during the bending downstroke, $\pi < \omega t < 2\pi$, with the extreme values reached at $\omega t = \pi/2$ and $\omega t = 3\pi/2$, respectively. Because the apex of the outer wing leading edge is not moving, the phase lags involved will be small. Consequently, the load distribution extremes will occur close to $\omega t = \pi/2$ and $\omega t = 3\pi/2$, and can be illustrated by the results in Fig. 26. Thus, during the bending upstroke, the lift is increased and thereby the bending moment, whereas during the downstroke lift and bending moment are decreased by the vortex interaction. In both cases the dynamic effect is destabilizing, driving the bending oscillations, in agreement with the experimental results¹¹.

It is essential that the designer recognize and understand the flow mechanism(s) causing dynamic instability for his particular vehicle. In the case of the transition-induced wing bending oscillations¹ (Figs. 1-3) it was suggested that this was a problem relegated to low Reynolds number flows, as on small high-performance gliders, or large transport aircraft with suction to achieve laminar flow. Quite to the contrary, the results¹ are in complete agreement with the general experience in regard to moving wall effects in both two- and three-dimensional flows¹⁰, showing that the closer the flow conditions are to the critical one, the higher the potential of the moving wall effect is. Consequently, the laminar flow extent was not extensive when the divergent oscillations occurred. Instead, transition to turbulent flow took place around mid-chord or earlier, and the problem becomes especially acute for high performance fighter-type aircraft with "flat-top" pressure distributions.

In the case of the bending wing oscillations caused by the interaction between two leading-edge vortices¹¹ (Figs. 11-13), not recognizing and understanding the flow mechanism causing the oscillation, the investigators focused all efforts on the outer, variable-sweep wing, trying numerous modifications (Fig. 27) without any success whatsoever. If the leading-edge stall strip had been applied to the inner wing glove and not the outer wing, chances are that the wing bending problem would have been eliminated, avoiding the present red-lining of the performance envelope of the aircraft.

When pondering the fact that the misinterpretation of the test results was in both cases made by people with impeccable technical qualifications, one realizes how great the need is for informal meetings of the work-shop-type, such as the present meeting.

REFERENCES

1. Mabey, D. G., Ashill, P. R. and Welsh, B. L., "Aeroelastic Oscillations Caused by Transitional Boundary Layers and Their Attenuation," J. Aircraft, Vol. 24, July 1987, pp. 463-469.
2. Ericsson, L. E., "Comment on Aeroelastic Oscillations Caused by Transitional Boundary Layers and their Attenuation," J. Aircraft, Vol. 25, Oct. 1988, pp. 975-976.
3. McCullough, G. B. and Gault, D. E., "Examples of Three Representative Types of Airfoil - Section Stall at Low Speed," NACA TN2502, 1951.
4. Liiva, J., Davenport, F. J., Gray, L. and Walton, I. C., "Two-Dimensional Tests of Airfoils Oscillating Near Stall," TR 68-13, April 1968, U.S. Army Aviation Labs, Fort Eustis, VA.
5. Ericsson, L. E. and Reding, J. P., "Stall Flutter Analysis," J. Aircraft, Vol. 10, Jan. 1973, pp. 5-13.
6. Halfman, R. L., Johnson, H. C. and Haley, S. M., "Evaluation of High-Angle-of-Attack Aerodynamic Derivative and Stall Flutter Prediction Techniques," NACA TN 2533, 1951.
7. Ericsson, L. E. and Reding, J. P., "Fluid Mechanics of Dynamic Stall, Part I. Unsteady Flow Concepts," J. Fluids and Structures, Vol. 2, 1988, pp. 1-33.
8. Modi, V. J. and Mokhtarian, F., "Joukovski Airfoil with Circulation Control," AIAA Paper No. 85-1772-CP, Aug. 1985.
9. Carta, F. O., "A Comparison of the Pitching and Plunging Response of an Oscillating Airfoil," NASA CR-3172, Oct. 1979.
10. Ericsson, L. E., "Moving Wall Effects in Unsteady Flow," J. Aircraft, Vol. 25, Nov. 1988, pp. 977-990.
11. Dobbs, S. K., Miller, G. D., and Stevenson, J. R., "Self-Induced Oscillation Wind Tunnel Test of a Variable Sweep Wing," AIAA Paper 85-0739-CP, April 1985.
12. Ericsson, L. E. and Reding, J. P., "Dynamic Stall at High Frequency and Large Amplitude," J. Aircraft, Vol. 17, No. 3, March 1980, pp. 136-142.
13. Lambourne, N. C. and Bryer, D. W., "The Bursting of Leading-Edge Vortices - Some observations and Discussion of the Phenomenon," Aer. Res. Council of Great Britain, R&M No. 3282 (1962).
14. Ericsson, L. E. and Reding, J. P., "Approximate Nonlinear Slender Wing Analysis," J. Aircraft, Vol. 14, No. 12, Dec. 1977, pp. 1107-1204.

15. Woodgate, L., "Measurements of the Oscillatory Pitching Moment Derivatives on a Delta Wing with Rounded Leading Edges in Incompressible Flow," Aer. Res. Council, Great Britain, R&M No. 3628, Pt 1, July 1968.
16. Krogmann, P., "Experimentelle und Theoretische Untersuchungen an Doppeldeltaflügeln," Bericht 68A35, Aerodynamische Versuchsanstalt, Göttingen, West Germany, July 1968.
17. Wendts, W. J. Jr. and McMahon, M.C., "An Experimental Investigation of the Flow Fields About Delta and Double-Delta Wings at Low Speeds," NASA CR-521, Aug. 1966.
18. Ericsson, L. E. and Reding, J. P., "Unsteady Aerodynamics of Slender Delta Wings at Large Angles of Attack," J. Aircraft, Vol. 12, No. 9, Sept. 1975, pp. 721-729.
19. Ericsson, L. E., "Dynamic Effects of Shock-Induced Flow Separation," Journal of Aircraft, Vol. 12, No. 2, February 1975, pp. 86-92. (ERRATA, J. Aircraft, Vol. 18, No. 7, July 1981, p.608)
20. Randall, D. G., "Oscillating Slender Wings with Leading-Edge Separation," The Aer. Quarterly, Vol. XVII, Nov. 1966, pp. 311-331.
21. Werlé, H., "Vortices from Very Slender Wings," La Recherche Aérospatiale, No. 109, Nov.-Dec. 1965, pp. 1-12.

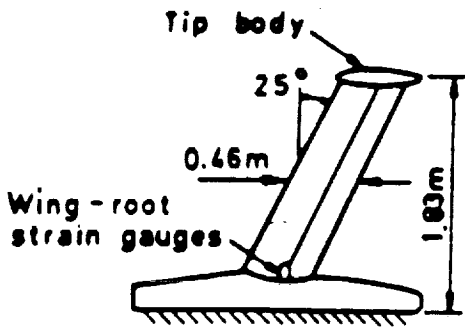


Fig. 1

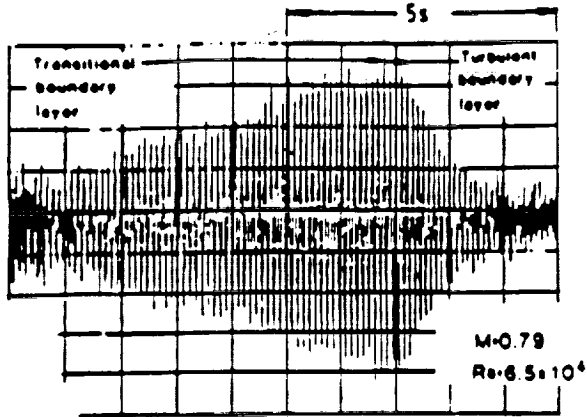


Fig. 3

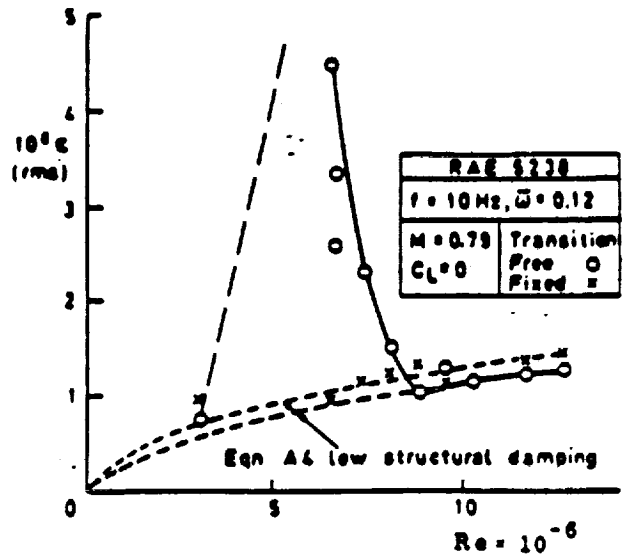


Fig. 2

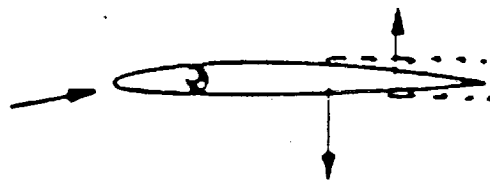


Fig. 4

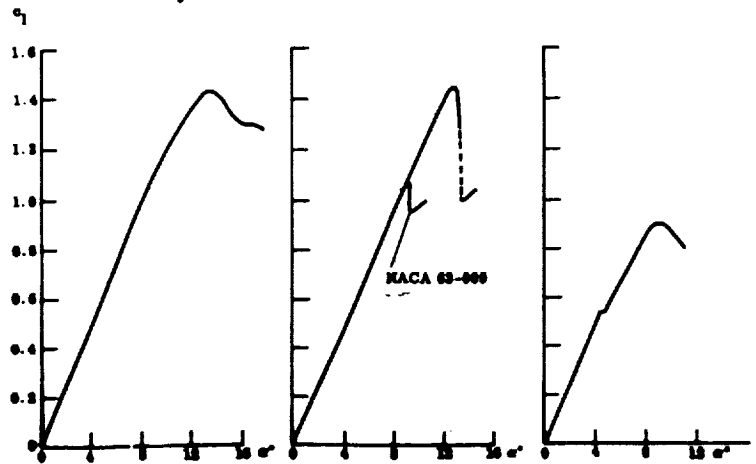
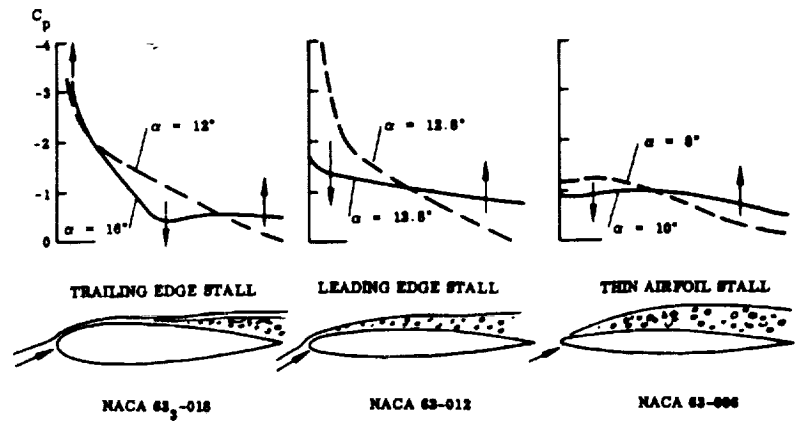


Fig. 5

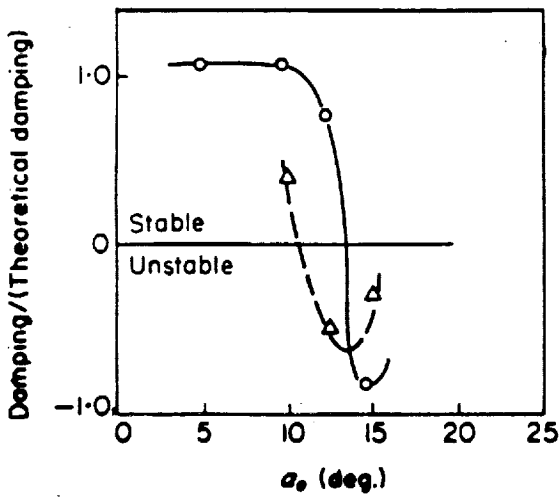


Fig. 6

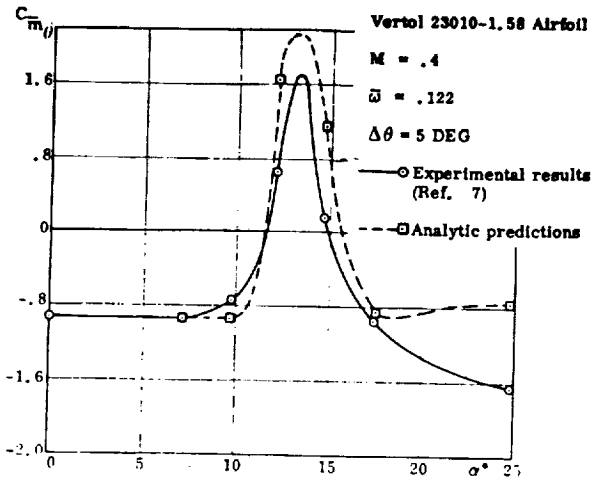


Fig. 7a

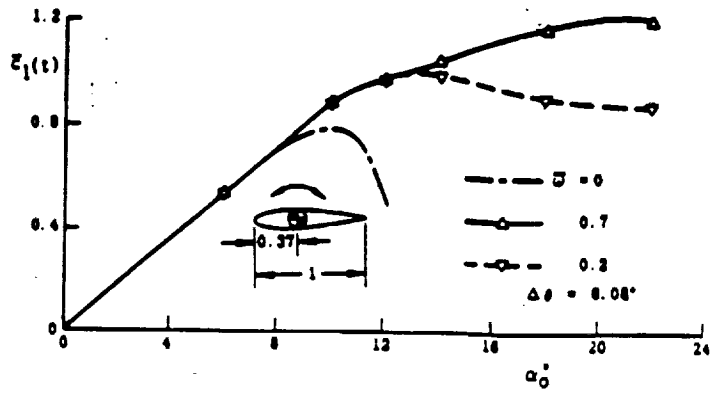


Fig. 7b

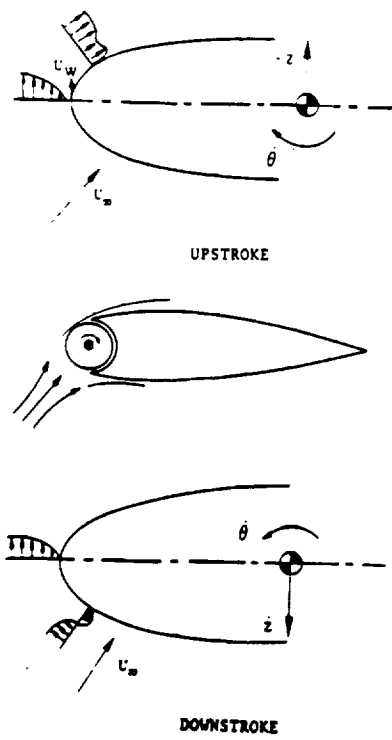


Fig. 8

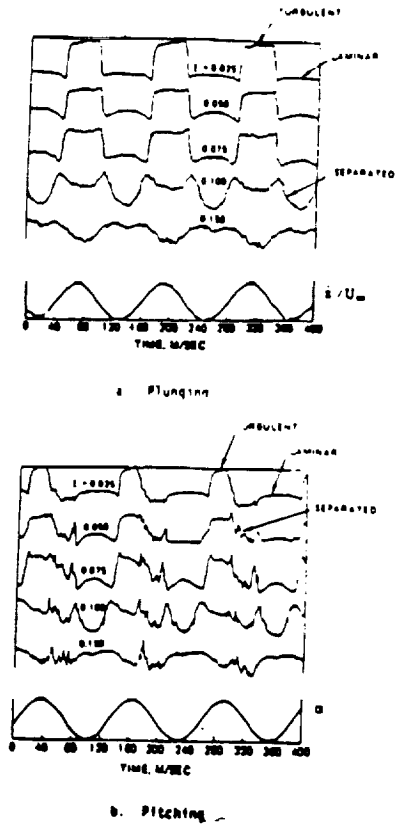


Fig. 9

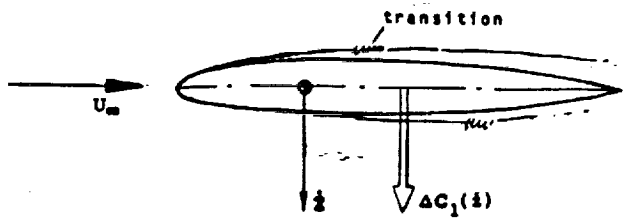
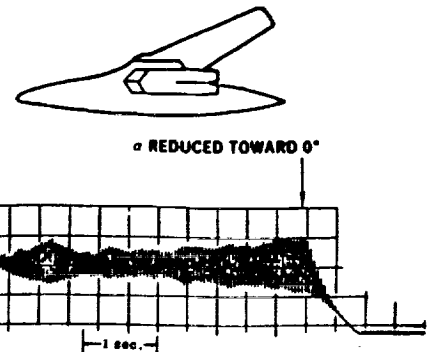


Fig. 10



SWEEP ANGLE, DEG	α POSE, DEG	MACH NUMBER	REYNOLDS NUMBER	TIP AMPLITUDE IN
87.1	7.30	0.975	5.9×10^6	0.976

Fig. 11

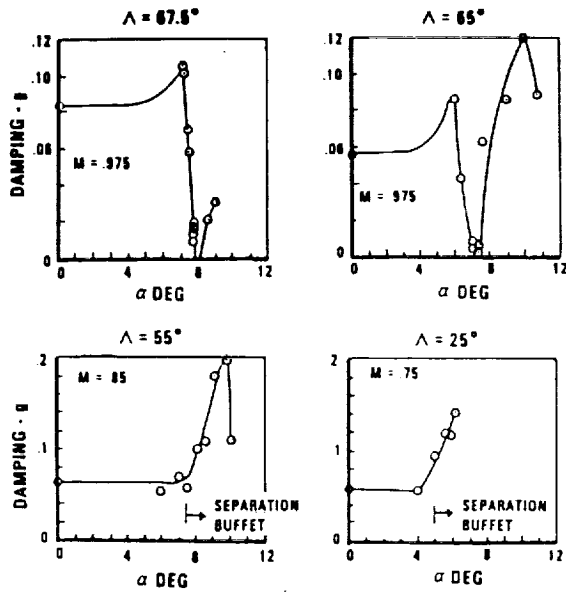


Fig. 12

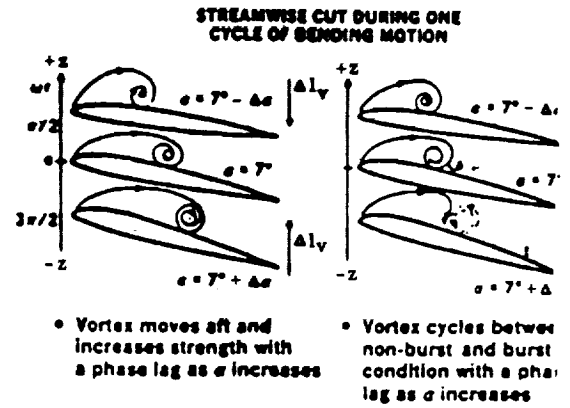


Fig. 14

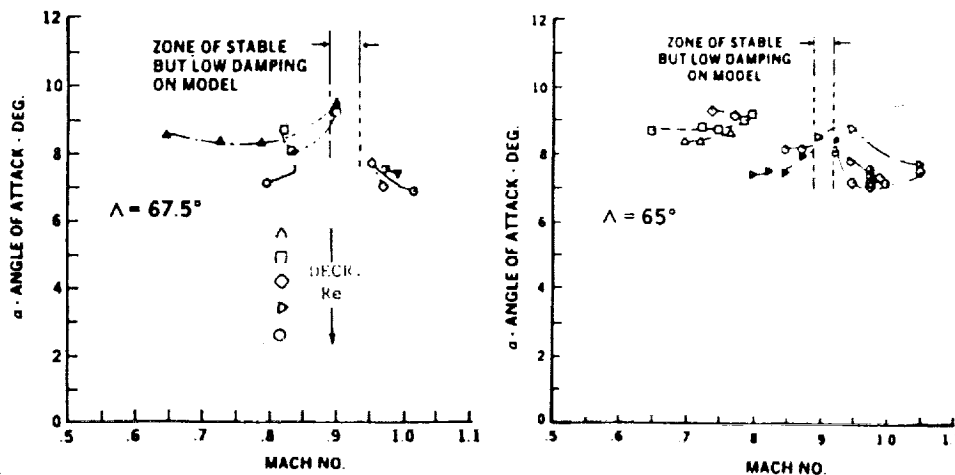


Fig. 13

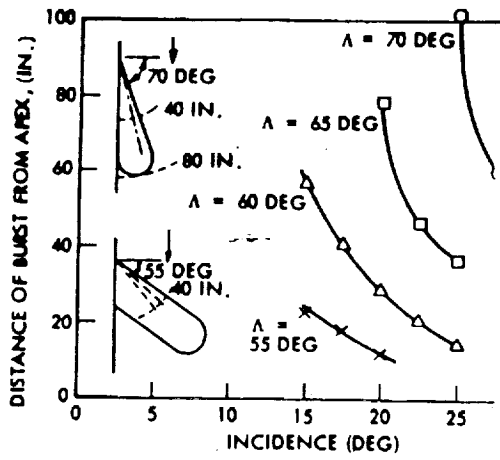


Fig. 15

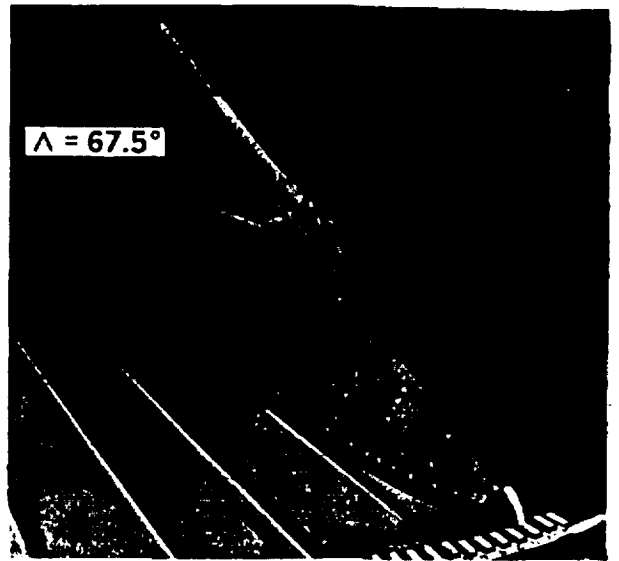


Fig. 16

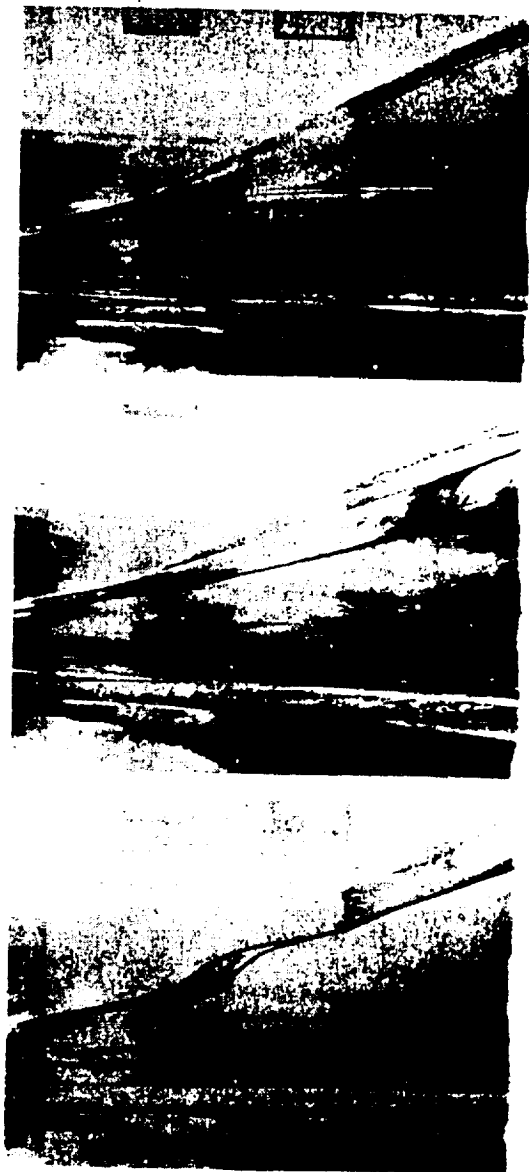


Fig. 19

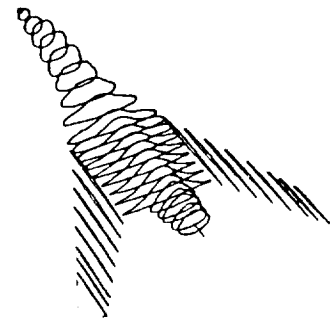


Fig. 17

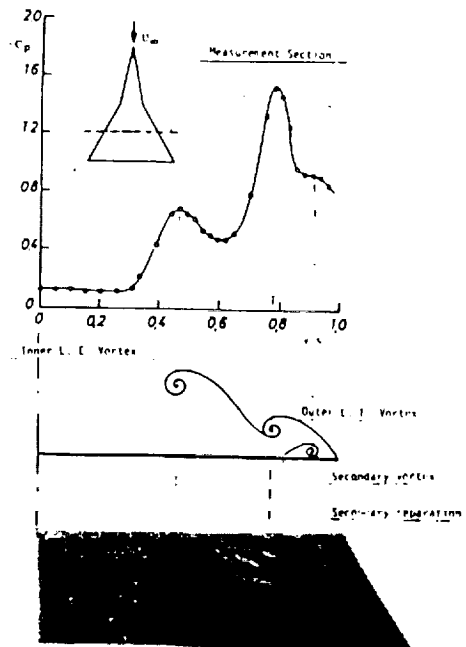


Fig. 18

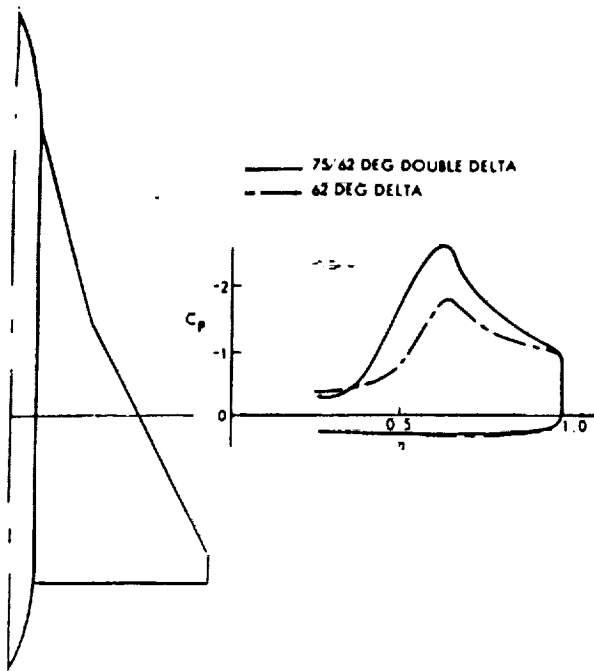


Fig. 20

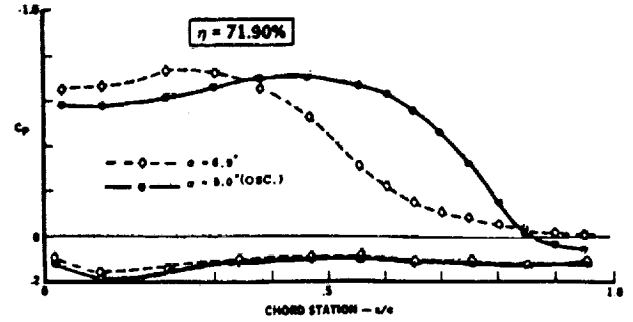


Fig. 21

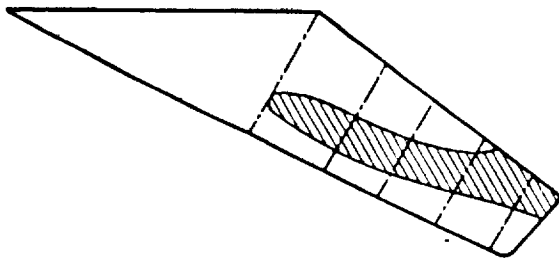


Fig. 22

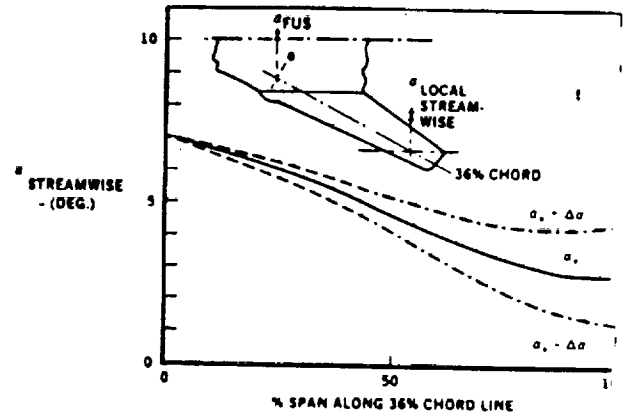


Fig. 23

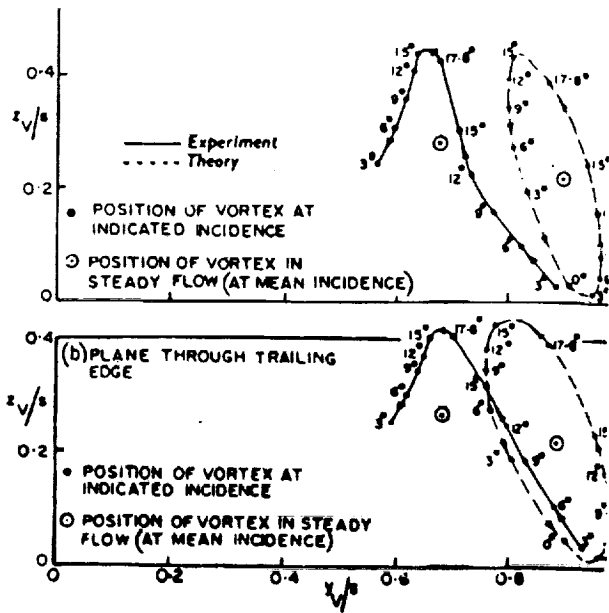


Fig. 24

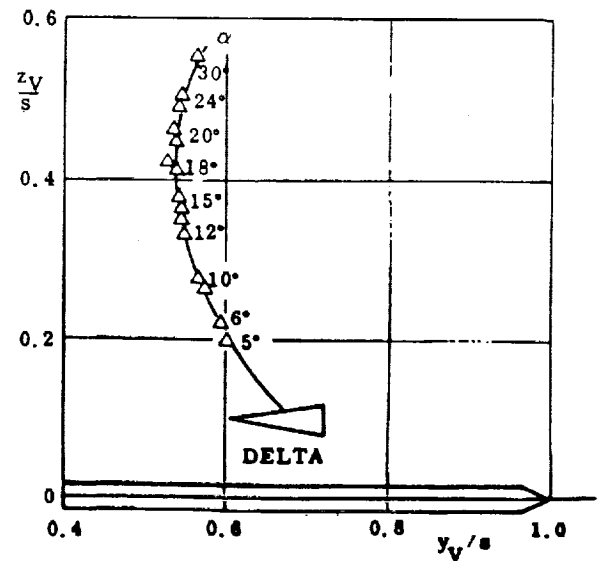


Fig. 25

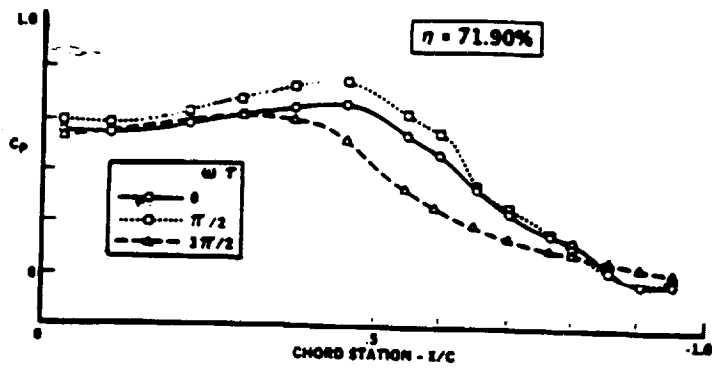


Fig. 26

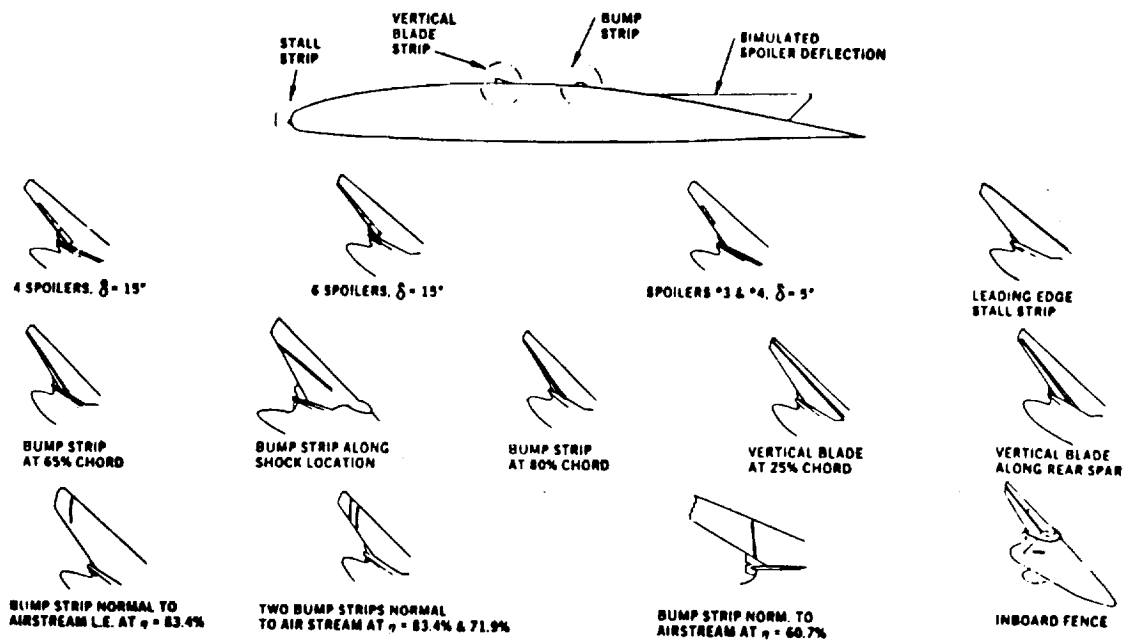


Fig. 27

